(Revision 1)

Kenorozhdestvenskayaite-(Fe), $Ag_6(Ag_4Fe_2)Sb_4S_{12}\square$: A new tetrahedrite group mineral containing a natural $[Ag_6]^{4+}$ cluster and its relationship to the synthetic ternary phosphide $(Ag_6M_4P_{12})M'_6$

KAI QU[1,2*], WEIZHI SUN[3], FABRIZIO NESTOLA[4], XIANGPING GU[5], ZEQIANG YANG[3], XIANZHANG SIMA[2], CHAO TANG[2], GUANG FAN[6] AND YANJUAN WANG[4,7*]

[1] School of Earth Sciences and Engineering, Nanjing University, Nanjing 210023, China

[2] Tianjin Center, China Geological Survey, Tianjin 300170, China.

[3] No.3 Institute of Geological and Mineral Resources Survey of Henan Geological Bureau, Xinyang 464000, China

[4] Department of Geosciences, University of Padova, Padova 35131, Italy.

[5] School of Geosciences and Info-Physics, Central South University, Changsha 410012, Hunan, China.

[6] Beijing Research Institute of Uranium Geology, Beijing 100029, China

[7] School of Earth Sciences and Resources, China University of Geosciences (Beijing), Beijing 100083, China.

*E-mail: qukai_tcgs@foxmail.com; wangyanjuan_cugb@foxmail.com

ABSTRACT

$[Ag_6]^{4+}$ clusters are extremely rare in nature (only found in Ag-rich tetrahedrite group minerals). Due to their remarkable structures and some promising applications, a few synthesis phases that contain octahedral $[Ag_6]^{4+}$ clusters have been reported in the area of material sciences. However, the kinds of natural conditions that promote the formation of subvalent hexasilver clusters in tetrahedrite group minerals are still unclear. Kenorozhdestvenskayaite-(Fe), ideally $Ag_6(Ag_4Fe_2)Sb_4S_{12}\square$ is a new tetrahedrite group mineral containing a natural $[Ag_6]^{4+}$ cluster and found in the Yindongpo gold deposit, Weishancheng ore field, Henan Province, China. This new species occurs at the edge of galena as anhedral grains of 2 to 20 μm in size and is associated with pyrargyrite, pyrrhotite, and siderite. Kenorozhdestvenskayaite-(Fe) is black in color with metallic luster. It is brittle with conchoidal fracture and has a calculated density of 5.329 g/cm^3. The empirical formula calculated on the basis of cation = 16 *apfu* is

$^{M(2)}Ag_6{}^{M(1)}(Ag_{2.41}Cu_{1.20}Fe_{1.84}Zn_{0.71})_{\Sigma 6.16}{}^{X(3)}(Sb_{3.82}As_{0.01})_{\Sigma 3.83}{}^{S(1)}S_{11.60}{}^{S(2)}\square$. It is cubic, with space group $I\bar{4}3m$, a = 10.7119(6) Å, V = 1229.1(2) Å^3, and Z = 2. Since kenorozhdestvenskayaite-(Fe) is a new tetrahedrite group mineral containing a natural $[Ag_6]^{4+}$ cluster, its structure is comparable to the synthetic ternary phosphide $(Ag_6M_4P_{12})M'_6$. The presence of the unusual mineral assemblages, i.e., pyrrhotite and pyrargyrite, as well as the other keno-endmember tetrahedrites, indicates a low $f(S_2)$ state for the mineralization stage, probably a result of the fluid boiling process in an open system that likely contributed to the formation of S-deficient tetrahedrites.

Keywords: Kenorozhdestvenskayaite-(Fe), silver cluster, $[Ag_6]^{4+}$ cluster, new mineral, tetrahedrite group, Yindongpo deposit

INTRODUCTION

The general structural formula of tetrahedrite-group minerals is $^{M(2)}A_6{}^{M(1)}(B_4C_2)^{X(3)}D_4{}^{S(1)}Y_{12}{}^{S(2)}Z$, where A = Cu^+, Ag^+, □ [vacancy], and $[Ag_6]^{4+}$ clusters; B = Cu^+ and Ag^+; C = Mn^{2+}, Fe^{2+}, Co^{2+}, Ni^{2+}, Cu^{2+}, Zn^{2+}, Cd^{2+}, Hg^{2+}, Cu^+, In^{3+}, and Fe^{3+}; D = Sb^{3+}, As^{3+}, Bi^{3+}, and Te^{4+}; Y = S^{2-} and Se^{2-}; and Z = S^{2-}, Se^{2-}, and □ (Biagioni et al. 2020a). As an ancient mineral group with 200 years of study history, tetrahedrite-group minerals are considered the most complex isotypic series among the sulfosalts in different types of ore deposits worldwide due to their multiplicity of iso- and heterovalent substitutions at different crystallographic positions (Johnson et al. 1988; Makovicky and Karup-Møller 1994; Moëlo et al. 2008). With the approval of the tetrahedrite group nomenclature by the Commission on New Minerals, Nomenclature and Classification of the International Mineralogical Association (IMA-CNMNC) (Biagioni et al. 2020a), in the last three years, an increasing number of new composition endmembers (i.e., Cd-, In-, Mn-, and Ni-endmembers) and special structure [$(Ag_6)^{4+}$] tetrahedrites have been discovered all worldwide. These newly discovered tetrahedrites and their crystal chemical properties can facilitate a new perspective for revealing the super-enrichment mechanism of critical metals in hydrothermal deposits (i.e., Cd, In, Se, and Te-endmembers; George et al. 2017) and provide important references in material science;

these tetrahedrites have potential large-scale thermoelectric (TE) applications in the area of waste heat recovery in the power-producing, processing, and automobile industries (Ni endmembers; Wang et al. 2023a, b). Promising material applications of subvalent hexasilver cluster endmembers have caused much research interest (Kikukawa et al. 2013; Wang et al. 2018; Sack et al. 2022), and this special structure only naturally occurs in four silver-rich tetrahedrites. Moreover, the kinds of natural conditions that promote the formation of silver clusters remains unclear.

Kenorozhdestvenskayaite-(Fe) has recently been discovered in the Yindongpo gold deposit, China. The new mineral and its name have been approved by the Commission on New Minerals, Nomenclature and Classification of the International Mineralogical Association (IMA-CNMNC) (IMA2022-001, Qu et al. 2022). Type material is deposited at the Geological Museum of China, No. 16, Yangrou Hutong, Xisi, Beijing 100031, People's Republic of China, under catalog number M16132. The root name "rozhdestsvenskayaite" [pronounced rozh-dest-ven-skayaite] is in honor of Russian mineralogist Irina Rozhdestvenskaya for her important contributions to mineralogy and to the crystal chemistry of the tetrahedrite group (Welch et al. 2018). The prefix (keno) and suffix (Fe) indicate vacancy at the S(2) site and the dominant C constituent, respectively. In fact, three pieces of silver-cluster-containing tetrahedrite [i.e., kenoargentotetrahedrite-(Zn), kenoargentotetrahedrite-(Fe), and kenorozhdestvenskayaite-(Fe)], and two unknown low-sulfur chalcogenides have been found in the Yindongpo gold deposit. The formation of these special minerals should be related to their special geological conditions. In this paper, the description of kenorozhdestvenskayaite-(Fe) is reported. In addition, its comparison to the isostructural ternary phosphide $(Ag_6M_4P_{12})M'_6$ and the origin of the naturally occurring silver clusters have been discussed.

GEOLOGICAL BACKGROUND

Kenorozhdestvenskayaite-(Fe) was found in the Yindongpo gold deposit (29°10'58.0" N, 92°17'47.6" E), which is in the Weishancheng Au-Ag-polymetallic ore field in the central part of the Qinling-Tongbai-Dabie Orogen, China (Fig. 1a, b). The Weishancheng Au-Ag-polymetallic ore belt is located in the Erlangping back-arc basin (Zhang et al. 2013). The Erlangping terrane, including the Erlangping Group and the Waitoushan Group, mainly contains Neoproterozoic–early Paleozoic volcanic-

sedimentary successions and associated intrusions and is located between the Kuanping Group and Qinling Group, separated by the Waxuezi fault and the Zhuyangguan-Xiaguan (Zhu-Xia) fault from north to south (Fig. 1c). The Yindongpo giant Au deposit, Poshan giant Ag deposit, and Yindongling large Ag-polymetallic deposits are found in carbonaceous quartz-sericite schists of the Neoproterozoic Waitoushan Group, occurring in the collapsed position of the axis and along the two limbs of the anticline (Zhang et al. 2011). The anticline was intruded by late Paleozoic Taoyuan granodiorite (390–357 Ma) and Mesozoic Liangwan monzogranite (128 Ma) (Zhang et al. 1999, 2000).

The Yindongpo deposit, with reserves of 56.26 t Au, is one of the most important gold deposits in central China. The main ore-controlling structures are the collapsed part at the turning end of the anticline, the conjugate thrust shear fracture zone on both wings, and the bedding compression fracture zone (Fig. 1d). The distribution of the orebodies is strictly controlled by carbonaceous wall rock. Most orebodies are hosted in the Middle-Waitoushan Formations (plagioclase-amphibole schist and carbonaceous quartz-sericite schist). This set of formations is considered the source layer for the deposit due to its high abundance of Au-Ag elements (Chen and Fu 1992; HBGMR, 1994). Previous studies indicate that the ore-forming process of the Yindongpo deposit can be divided into three stages, corresponding to silicification, sericitization, and carbonation and chloritization. Among them, the second (sericitization) stage is the main ore-forming stage, characterized by containing large amounts of galena, sphalerite, chalcopyrite, and native gold (Zeng et al. 2016; Zhang et al. 2011, 2013). Sericite separates from ore rock range in age from 171.8–119.5 Ma based on K-Ar and Ar-Ar geochronology, indicating that mineralization occurred during the Mesozoic collisional orogeny (Zhang et al. 2013).

OCCURRENCE AND PARAGENESIS

Kenorozhdestvenskayaite-(Fe) is found in massive sulfide ores and is associated with sphalerite, galena, chalcopyrite, pyrrhotite, pyrite, pyrargyrite, kenoargentotetrahedrite-(Fe), kenoargentotetrahedrite-(Zn), siderite, kutnohorite, rhodochrosite, and two unknown Ag chalcogenide phases (Fig. 2). Kenorozhdestvenskayaite-(Fe) commonly occurs as euhedral to anhedral grains at the edge of the galena crystals (Fig. 2a, b) or the narrow part of the galena grains (Fig. 2a, e), equant crystals up to 20 μm in size with black color, and the luster is metallic. It is brittle,

with an indistinct cleavage. Due to the small amount of available material and the intergrowth of other phases on the micron scale, its density was not measured. The calculated density, based on the empirical formula and unit-cell volume refined from single-crystal X-ray diffraction (XRD) data, is 5.329 g/cm^3. Kenorozhdestvenskayaite-(Fe) is opaque in transmitted light and shows a greenish gray color in reflected light. Internal reflections are brown–red.

RAMAN SPECTROSCOPY

The Raman spectrum of kenorozhdestvenskayaite-(Fe) was collected using a Renishaw in Via micro-Raman system with a laser with a frequency of 532 nm (power: 4 mW, spatial resolution: 1 μm) and equipped with a motorized x–y stage and a Leica microscope with a 50× objective (Tianjin Center, China Geological Survey, China). The back-scattered Raman signal was collected, and the spectra were obtained from the polished thin section. The typical kenorozhdestvenskayaite-(Fe) Raman spectrum from 150 to 1200 cm^{-1} is shown in Fig. 3. The major Raman bands observed at 353 cm^{-1} can be assigned to Sb–S stretching vibrations. The weak intensity shoulder at 345 cm^{-1} is attributed to antisymmetric stretching, while the symmetric bending and antisymmetric bending modes appear as weak peaks at 311 cm^{-1} and 287 cm^{-1}, respectively. Lattice vibration is found at 157 cm^{-1}.

CHEMICAL COMPOSITION

Quantitative electron microprobe (EPMA) analyses of kenorozhdestvenskayaite-(Fe) were carried out with a JXA-8100 electron microprobe at 20 kV and 10 nA with a beam diameter of 1 μm (Beijing Research Institute of Uranium Geology, China). Standards and the following X-ray lines were used: metallic Ag (Ag*K*α), chalcopyrite (Cu*K*α and S*K*α), pyrite (Fe*K*α), ZnS (Zn*K*α), Sb_2S_3 (Sb*L*α), and GaAs (As*L*α).

Electron microprobe analysis data (average of 7 spot analyses) are given in Table 1. The empirical formula calculated on the basis of 16 cations per formula unit is $^{M(2)}Ag_6{}^{M(1)}(Ag_{2.41}Cu_{1.20}Fe_{1.84}Zn_{0.71})_{\Sigma 6.16}{}^{X(3)}(Sb_{3.82}As_{0.01})_{\Sigma 3.83}{}^{S(1)}S_{11.60}{}^{S(2)}\square$. The ideal formula is $Ag_6(Ag_4Fe_2)Sb_4S_{12}\square$, which requires Ag 52.30, Fe 5.42, Sb 23.62, S 18.66, and a total of 100 wt.%.

X-RAY CRYSTALLOGRAPHY AND STRUCTURE DETERMINATION

The studied material is a nearly equidimensional crystal (approximately 5 × 4 × 3 μm), which was extracted from the polished thin section by using an FEI Helios NanoLab 600i DualBeam SEM/FIB system containing a high-resolution field emission scanning electron microscope (FESEM) with a focused Gallium ion beam (FIB) microscope (Institute of Microstructure and Property of Advanced Materials, Beijing University of Technology, China). Single-crystal XRD was carried out with a Rigaku XtaLAB Synergy diffractometer equipped with a hybrid pixel array detector and Cu*K*α radiation at 50 kV and 1 mA (School of Geosciences and Info-Physics, Central South University, China). The intensity data were corrected for X-ray absorption using the multiscan method, and empirical absorption correction was performed using CrysAlisPro program spherical harmonics (Rigaku Oxford Diffraction, 2021), implemented in the SCALE3 ABSPACK scaling algorithm. The refined unit-cell edge is a = 10.7119(6) Å and V = 1229.1(2) Å^3; the space group is $I\bar{4}3m$. The crystal structure was solved and refined using SHELX (Sheldrick 2015) and Olex2 software (Dolomanov et al. 2009). Scattering factors for neutral atoms were used initially: Ag vs. Cu at *M*(2), Sb at *X*(3), S at S(1) and S(2) sites. Due to the similarity of the scattering factors of Cu, Fe, and Zn, the tetrahedrally coordinated site *M*(1) was appropriately fixed to minimize R_1 factor and achieve good agreement with the chemical data. After several cycles of anisotropic refinement for all the atoms, R_1 converged to 0.0355 for 221 independent reflections with $F_o > 4\sigma (F_o)$ and 19 refined parameters (see Online Materials[1] for CIF file).

Powder XRD data could not be collected due to the extremely small size of the crystal. The pattern provided in Table 2 was calculated using VESTA software (Momma and Izumi 2011) based on the structural model.

Results and Discussion

Crystal structure description

Kenorozhdestvenskayaite-(Fe) is isostructural with kenoargentotetrahedrite-(Fe) and other members of the tetrahedrite group (Fig. 4). As described by Rozhdestvenskaya et al. (1993) and Welch et al. (2018), freibergite [renamed kenoargentotetrahedrite-(Fe) by Biagioni et al. (2020a)] has homotypic relations with the other members of the tetrahedrite group, with the occurrence of the $[Ag_6]^{4+}$ cluster replacing the S(2)Ag_6 octahedron, according to the substitution mechanism $6^{M(2)}Ag^{+} + {}^{S(2)}S^{2-} = {}^{M(2)}[Ag_6]^{4+} + {}^{S(2)}$

185 □.

186 The result of structure refinement for kenorozhdestvenskayaite-(Fe) shows that it
187 could be characterized by Ag-dominance in the B constituent of kenoargentotetrahedrite-
188 (Fe), or $[Ag_6]^{4+}$ cluster at the *M*(2) site, meanwhile, vacancy-dominance at the S(2) site of
189 *rozhdestvenskayaite-(Fe)* (not approved yet). In kenorozhdestvenskayaite-(Fe), *M*(2)–S(1)
190 and *M*(2)–S(2) have average bond distances of 2.550(6) Å and 2.011(3) Å, respectively.
191 To maintain charge balance, the metallically bonded Ag_6 group needs to exist with an
192 aggregate formal charge of +4. Evidence for Ag–Ag bonding can be found in the *M*(2)–
193 *M*(2) distance of 2.844 Å of kenorozhdestvenskayaite-(Fe), consistent with the Ag–Ag
194 distances (2.841 Å, 2.890 Å) in kenoargentotetrahedrite-(Fe) and
195 kenoargentotetrahedrite-(Zn), respectively (Welch et al. 2018; Qu et al. 2021). These Ag–
196 Ag distances were similar to those of metallic silver (2.85 Å) and significantly shorter
197 than the sum of the van der Waals radii of silver atoms (3.44 Å), indicating the presence
198 of metallic bonding in these octahedral groups. This feature of kenorozhdestvenskayaite-
199 (Fe) is markedly different from the rozhdestvenskayaite-(Zn). In the former, S(2) site is
200 vacant, whereas in the latter the site is occupied, and the Ag–Ag distances is 3.230 Å
201 (Welch et al. 2018) (Table 3). The occurrence of the $[Ag_6]^{4+}$ cluster also agrees with the
202 calculated bond-valence sum (BVS) of 0.642 valence units (v.u.) (theor. = 0.667 v.u.)
203 (Table 4). The presence of the $[Ag_6]^{4+}$ cluster results in a reduction of the $S(2)M(2)_6$
204 octahedral with a volume of 10.84 $Å^3$, which is compared with the values of
205 kenoargentotetrahedrite-(Fe) and kenoargentotetrahedrite-(Zn) (10.81 $Å^3$, Welch et al.
206 2018; 11.38 $Å^3$, Qu et al. 2021) and distinguished from rozhdestvenskayaite-(Zn) (oct.
207 vol. 15.88 $Å^3$) (Welch et al. 2018). The $[Ag_6]^{4+}$ cluster is probably in the form
208 $[(Ag^{1+})_4(Ag^0)_2]$ which would indicate two types of Ag atoms different bonding with the
209 surrounding S^{2-} ligands by ionic-covalent and metallic bonds, or as $[(Ag^{1+})_{2/3}(Ag^0)_{1/3}]_6$, in
210 which case six equivalent bonds of a mixed covalent-metallic character. Although it is
211 expected that the latter should be more realistic, further investigations are still desirable
212 to highlight this aspect of the chemical bonding mechanism in subvalent hexasilver
213 clusters.

214 The tetrahedrally coordinated *M*(1) site of kenorozhdestvenskayaite-(Fe) has bond
215 length [*M*(1)–S(1)] of 2.439(4) Å, slightly shorter than the observed bond length [2.496(2)

Å] for rozhdestvenskayaite-(Zn) reported by Welch et al. (2018); this result is consistent with chemical and crystal data showing that there is less Ag at the *M*(1) site of the studied kenorozhdestvenskayaite-(Fe). Since Ag replaces Cu at the *M*(1) site, the bond distances are longer than those in kenoargentotetrahedrite-(Fe) [2.333(1) Å, Welch et al. 2018] and kenoargentotetrahedrite-(Zn) [2.343(2) Å, Qu et al. 2021] (Table 3). The large effect on the unit-cell volume caused by the difference in the ionic radii of $^{IV}Ag^{+}$ (1.00 Å) and $^{IV}Cu^{+}$ (0.60 Å) (Shannon 1976) has been discussed by Welch et al. (2008). Compared to rozhdestvenskayaite-(Zn) with the unit cell parameters of 10.9845(7) Å, the differences in the values are mainly due to the S fully occupying the S(2) site. In contrast, the corresponding unit cell value of kenoargentotetrahedrite-(Fe) is 10.4930(4) Å, which shows the larger difference from kenorozhdestvenskayaite-(Fe) and is caused by Ag cations dominating at *M*(1) sites. The BVS of the *M*(1) site is 1.697 v.u. and has a higher deviation from the theoretical value (1.333 v.u.), which appears to be a common phenomenon in tetrahedrite group minerals (Biagioni et al. 2020*b*, 2021, 2022; Sejkora et al. 2021, 2022).

The *X*(3)–S(1) averaged bond distance is 2.428(6) Å, which is consistent with the reported bond distance of tetrahedrite series minerals (Johnson and Burnham 1985; Rozhdestvenskaya et al. 1993; Welch et al. 2018; Biagioni et al. 2020*b*). The BVS of the *X*(3) site is 3.184 v.u., which is consistent with the presence of Sb^{3+}.

S(1) site is fourfold coordinated and bonded to two *M*(1), one *M*(2), and one *X*(3), with a BVS of 2.23 v.u. Vacancy domination at S(2) site was observed during the structure refinement, the ($\square_{0.9}S_{0.1}$) occupancy is consistent with chemical data determined by EPMA. The high apparent thermal motion at the S(2) site is a common phenomenon for the reported silver-rich tetrahedrite varieties; its mechanism is potentially related to site disorder caused by Ag occupancy at the *M*(2) site (Peterson and Miller 1986).

Relationship to the synthetic ternary phosphides ($Ag_6M_4P_{12}$)M'_6

To our knowledge, $[Ag_6]^{4+}$ clusters are extremely rare in nature (thus far, only found in Ag-rich tetrahedrite group minerals) and have only been discovered in the last few years. In contrast, a few phases of silver-rich oxides that contain octahedral $[Ag_6]^{4+}$ clusters, i.e., Ag_3O (Beesk et al. 1981), Ag_5GeO_4 (Jansen and Linke 1992), and Ag_5SiO_4 (Linke and Jansen 1994), have been reported in the area of material sciences since the

1980s (Derzsi et al. 2021). Due to their remarkable structures and some promising applications, high-nuclearity silver clusters with an octahedrally shaped $[Ag_6]^{4+}$ kernel have been appealing synthetic targets during the last decade (Kikukawa et al. 2013; Wang et al. 2018). In addition to the above synthetic materials, the structural model of kenorozhdestvenskayaite-(Fe), as well as the other keno-members of the tetrahedrite group mineral, is identical to the synthetic ternary phosphides $[Ag_6M^{II}_4P_{12}]M^{IV}_6$ (M^{II} = Ge, Sn; M^{IV} = Ge, Si) (Bullett and Dawson 1986; Bullett and Witchlow 1986; Comins et al. 1986; Gmelin et al. 1989; Nuss et al. 2017); they are both cubic, have the same space group ($I\bar{4}3m$) and Wyckoff position and are practically unoccupied in the center of the regular octahedral configuration of the $[Ag_6]^{4+}$ cluster. The cluster forms Ag–Ag metal–metal bonds with Ag–Ag distances of 2.844(4) Å and 2.8379(7) Å (Table 5), and its surroundings are covalently bonded and pyramidally coordinated in kenorozhdestvenskayaite-(Fe) $[SbS_3]$ and $(Ag_6Ge_4P_{12})Ge_6$ $[GeP_3]$, respectively. The electronic structure of the synthetic $(Ag_6M^{2+}_4P_{12})M^{4+}_6$ in the study by Nuss et al. (2017) indicated that the lone pair at the M^{2+} site toward the triangular faces of the Ag_6 octahedron made a condition for the bonding in subvalent hexasilver clusters. Although the ^{III}Sb radius (0.76 Å) is significantly larger than that of ^{III}As (0.56 Å) in tetrahedrite group minerals, it should be noted that, in addition to the three known Sb-dominance keno-member tetrahedrites [kenoargentotetrahedrite-(Fe), kenoargentotetrahedrite-(Zn), and kenorozhdestvenskayaite-(Fe)], there is also an As-dominance phase, i.e., kenoargentotennantite-(Fe), which has been found in nature. Therefore, in the absence of synthetic experimental confirmation thus far, it is still unclear whether the radius of the cation at the *X*(3) site could play a crucial role in promoting the formation of silver clusters in Ag-rich tetrahedrites (Fig. 5).

Genesis of the silver cluster in tetrahedrite

Taking into account the potential genetic indication and reference value in the fields of mineral deposits and material sciences, respectively, the kinds of natural conditions that promote the formation of silver clusters in some tetrahedrites but not in others needs to be considered. Although previous studies from the mid-1970s already discovered that the unit-cell edge of some silver-rich tetrahedrites (freibergite) decreased with increasing silver content (Riley 1974; Samusikov et al. 1988; Balitskaya et al. 1989),

Rozhdestvenskaya et al. (1993) first demonstrated that *freibergite* may contain silver clusters instead of the S(2)-centered Ag_6 octahedron of the traditional tetrahedrite group minerals. This abnormal trend appeared to show that when the silver content is > 4 apfu, the decrease in the unit-cell edge with increasing Ag content has a linear relationship with a certain negative correlation (Moëlo et al. 2008; Biagioni et al. 2020a), which implies that the occurrence of silver clusters may be related to the ratio of Ag/Cu. However, some of the freibergite series tetrahedrite (Ag > 8 apfu), i.e., kenorozhdestvenskayaite-(Fe), did not evidently meet this prediction. Therefore, other unknown reasons should restrict the formation of silver clusters. When compared to kenorozhdestvenskayaite-(Fe) and rozhdestvenskayaite-(Zn), the latter's octahedral cluster of Ag atoms opens up and contains S atom at its center; thus, the promotion mechanism of silver cluster formation could potentially be related to sulfur fugacity in mineral formation.

Mineral assemblages can be used as indicators of ore-forming conditions. In this respect, it is worth noting that, compared to pyrite, the most abundant sulfide in the epithermal hydrothermal gold-silver polymetallic deposits, silver cluster-containing tetrahedrite is predominantly associated with pyrrhotite in the Yindongpo deposit (Fig. 2). Pyrrhotite is commonly used to estimate the fugacity of sulfur in natural and experimental systems (Mengason et al. 2010). The $\log fS_2$ calculated based on the component of pyrrhotite ranges from -11.40 to -8.83 (mean -10.03) (Table 6), indicating that these sulfur-deficient minerals formed under low sulfur fugacity conditions.

The low sulfidation state was potentially induced by extensive H_2S loss during boiling or by the influx of meteoric water with a low S content (Lynch 1989). Previous studies of fluid inclusions in the Yindongpo deposit showed that fluid boiling occurred during the second stage of the ore-forming period (Zhang et al. 2009, 2013; Zeng et al. 2016), and siderite frequently appeared together with kenorozhdestvenskayaite-(Fe), pyrargyrite, and pyrrhotite in the studied hand specimen, whose formation is considered closely related to the boiling event (Lynch et al. 1990). Furthermore, hydrogen–oxygen isotope studies of the Yindongpo deposit indicated that the ore-forming fluids in the stage were superimposed on the transformation of atmospheric water (Zhang et al. 2013). Therefore, the above two effects potentially played an important role in reducing the sulfur fugacity of the ore-forming system. This process mainly occurred in the

transformation stage of the structural system from compression to extension. The opening of these structures also facilitated fluid immiscibility or boiling and mixing with circulating meteoric water, resulting in the rapid precipitation of sulfides. The desulfurization processes of fluid boiling and sulfide precipitation consumed a large amount of S in the ore-forming fluid, and pyrrhotite, as well as the keno-endmember tetrahedrites were finally formed in the low sulfur fugacity environment.

Implications

Kenorozhdestvenskayaite-(Fe), an extremely rare $[Ag_6]^{4+}$ cluster containing tetrahedrite group mineral, formed in a low sulfur fugacity environment through a fluid boiling-associated event. Since the Ag–Ag metal bond in tetrahedrite was not fully understood until recent years, most sulfur-deficient tetrahedrites reported in the previous literature were usually attributed to analytical uncertainty in the electron microprobe analysis (Repstock et al. 2016; Wang et al. 2018; Sejkora et al. 2021). From this point of view, it is necessary to re-investigate some reported sulfur-deficient and silver-rich tetrahedrites; as a result, new keno-endmember tetrahedrites could potentially be discovered and the origin of natural silver clusters and the genesis of ore deposits could be more fully understood.

Acknowledgements

The help comments from Adam Pieczka, Sergey Krivovichev, associate editor Kimberly Tait, and technical editor are greatly appreciated. This study was financially supported by Geological exploration project of Henan Geological and Mineral Exploration and Development Bureau (Yudikuang202205), National Key R&D Programmes (92062220), China Geological Survey Project (DD20190121), National Natural Science Foundation of China (42072054), and China Scholarship Council (CSC) 202106400047, 202108575009).

References cited

Balitskaya, O.V., Mozgova, N.N., Borodaev, Y.S., Efimova, A.V., and Tsepin, A.I. (1989) Evolution of the unit-cell parameter of fahlores with their silver content. Izvestiya Akademii Nauk SSSR, Seriya Geologicheskaya, 9, 112–120 (in Russian).

Beesk, W., Jones, P.G. Rumpel, H., Schwarzmann, E., and Sheldrick, G.M. (1981) X-ray crystal structure of Ag_6O_2. Chemical Communication, 14, 664–665.

340 Biagioni, C., George, L.L., Cook, N.J., Makovicky, E., Moëlo, Y., Pasero, M., Sejkora, J.,
341 Stanley, C.J., Welch, M.D., and Bosi, F. (2020a) The tetrahedrite group:
342 Nomenclature and classification. American Mineralogist, 105, 109–122.
343 Biagioni, C., Sejkora, J., Musetti, S., Velebil, D., and Pasero, M. (2020b). Tetrahedrite-
344 (Hg), a new 'old'member of the tetrahedrite group. Mineralogical Magazine, 84,
345 584–592.
346 Biagioni, C., Sejkora, J., Raber, T., Roth, P., Moëlo, Y., Dolníček, Z., and Pasero, M.
347 (2021) Tennantite-(Hg), $Cu_6(Cu_4Hg_2)As_4S_{13}$, a new tetrahedrite-group mineral
348 from the Lengenbach quarry, Binn, Switzerland. Mineralogical Magazine, 85,
349 744–751.
350 Biagioni, C., Kasatkin, A., Sejkora, J., Nestola, F., and Škoda, R. (2022) Tennantite-(Cd),
351 $Cu_6(Cu_4Cd_2)As_4S_{13}$, from the Berenguela mining district, Bolivia: the first Cd-
352 member of the tetrahedrite group. Mineralogical Magazine, 86, 834–840.
353 Brese, N.E., and O'Keeffe, M. (1991) Bond-valence parameters for solids. Acta
354 Crystallographica, B47, 192–197.
355 Brown, I.D. (1977) Predicting bond lengths in inorganic crystals. Acta Crystallographica
356 Section B: Structural Crystallography and Crystal Chemistry, 33, 1305–1310.
357 Bullett, D.W., and Dawson, W.G. (1986) Bonding relationships in some ternary and
358 quarternary phosphide and tetrahedrite structures: $[Ag_6M_4P_{12}]M'_6$, $Cu_{12+x}Sb_4S_{13}$
359 and $Cu_{14-x}Sb_4S_{13}$, $Ln_6Ni_6P_{17}$. Journal of Physics C: Solid State Physics, 19, 5837–
360 5847.
361 Bullett, D.W., and Witchlow, G.P. (1986) Bonding in semiconducting Ag_6-cluster
362 compounds: $[Ag_6Ge_4P_{12}]Ge_6$, $[Ag_6Sn_4P_{12}]Ge_6$, and $[Ag_6Sn_4P_{12}]Si_6$. Physical
363 Review B, 33, 2429–2431.
364 Chen, Y.J., and Fu, S.G. (1992) Gold Mineralization in West Henan, China.
365 Seismological Press, Beijing, pp. 1–234 (in Chinese with English abstract).
366 Comins, J.D., Heremans, C., Salleh, M.D., Saunders, G.A., and Hönle, W. (1986) Elastic
367 behaviour and vibrational anharmonicity of the cluster compound $(Ag_6Sn_4P_{12})Ge_6$.
368 Journal of materials science letters, 5, 1195–1197.
369 Derzsi, M., Uhliar, M., and Tokár, K. (2021) Ag_6Cl_4: the first silver chloride with rare
370 Ag_6 clusters from an ab initio study. Chemical Communications, 57, 10186–

10189.

Dolomanov, O.V., Bourhis, L.J., Gildea, R.J., Howard, J.A.K., and Puschmann, H. (2009) A complete structure solution, refinement and analysis program. Journal of Applied Crystallography, 42, 339–341.

George, L.L., Cook, N.J., and Ciobanu, C.L. (2017) Minor and trace elements in natural tetrahedrite-tennantite: Effects on element partitioning among base metal sulphides. Minerals, 7, 17.

Gmelin, E., Hönle, W., Mensing, C., von Schnering, H. G., and Tentschev, K. (1989) Chemistry and structural chemistry of phosphides and polyphosphides 51. Journal of thermal analysis, 35, 2509–2527.

Henan Bureau of Geology and Mineral Resources (HBGMR) (1994) Detailed Geological Investigation Report on Western Part of the Yindongpo Gold Deposit in Tongbai County, Henan Province, Xinyang. pp. 1–198 (in Chinese).

Jansen, M., and Linke, C. (1992) Ag_5GeO_4, a new semiconducting oxide. Angewandte Chemie International Edition in English, 31, 653–654.

Johnson, M.L., and Burnham, C.W. (1985) Crystal structure refinement of an arsenic-bearing argentian tetrahedrite. American Mineralogist, 70, 165–170.

Johnson, N.E., Craig, J.R., and Rimstidt, J.D. (1988) Crystal chemistry of tetrahedrite. American Mineralogist, 73, 389–397.

Kikukawa, Y., Kuroda, Y., Suzuki, K., Hibino, M., Yamaguchi, K., and Mizuno, N. (2013). A discrete octahedrally shaped $[Ag_6]^{4+}$ cluster encapsulated within silicotungstate ligands. Chemical Communications, 49, 376–378.

Linke, C., and Jansen, M. (1994) Subvalent ternary silver oxides: synthesis, structural characterization, and physical properties of pentasilver orthosilicate, Ag_5SiO_4. Inorganic Chemistry, 33, 2614–2616.

Lynch, J.V.G. (1989) Large–scale hydrothermal zoning reflected in the tetrahedrite–freibergite solid solution, Keno Hill Ag–Pb–Zn district, Yukon. The Canadian Mineralogist, 27, 383–400.

Lynch, J.V.G., Longstaffe, F.J., and Nesbitt, B.E. (1990) Stable isotopic and fluid inclusion indications of large-scale hydrothermal paleoflow, boiling, and fluid mixing in the Keno Hill Ag-Pb-Zn district, Yukon Territory, Canada. Geochimica

et Cosmochimica Acta, 54, 1045–1059.

Makovicky, E., and Karup-Møller, S. (1994) Exploratory studies on substitution of minor elements in synthetic tetrahedrite. Part I. Substitution by Fe, Zn, Co, Ni, Mn, Cr, V and Pb. Unit-cell parameter changes on substitution and the structural role of "Cu^{2+}". Neues Jahrbuch für Mineralogie Abhandlungen, 167, 89–123.

Mengason, M.J., Piccoli, P.M., and Candela, P. (2010) An evaluation of the effect of copper on the estimation of sulfur fugacity (f_{S2}) from pyrrhotite composition. Economic Geology, 105, 1163–1169.

Moëlo, Y., Makovicky, E., Mozgova, N.N., Jambor, J.L., Cook, N., Pring, A., Paar, W., Nickel, E.H., Graeser, S., Karup-Møller, Žunic, T.B., Mumme, W.G., Vurro, F., Topa, D., Bindi, L., Bente, K., and Shimizu, M. (2008) Sulfosalt systematics: a review. Report of the sulfosalt sub-committee of the IMA Commission on Ore Mineralogy. European Journal of Mineralogy, 20, 7–46.

Momma, K., and Izumi, F. (2011) VESTA 3 for three-dimensional visualization of crystal, volumetric and morphology data. Journal of Applied Crystallography, 44, 1272–1276.

Nuss, J., Wedig, U., Xie, W., Yordanov, P., Bruin, J., Hübner, R., Weidenkaff, A., and Takagi, H. (2017) Phosphide–tetrahedrite $Ag_6Ge_{10}P_{12}$: thermoelectric performance of a long-forgotten silver-cluster compound. Chemistry of Materials, 29, 6956–6965.

Peterson, R.C., and Miller, I. (1986) Crystal structure and cation distribution in freibergite and tetrahedrite. Mineralogical Magazine, 50, 717–721.

Qu, K., Sima, X.Z., Zhou, H.Y., Xiao, Z.B., Tu, J.R., Yin, Q.Q., Liu, X., and Li, J.H. (2019) In situ LA-MC-ICP-MS and ID-TIMS U-Pb ages of bastnäsite-(Ce) and zircon from the Taipingzhen hydrothermal REE deposit: new constraints on the Later Paleozoic granite-related U-REE mineralization in the North Qinling Orogen, Central China. Journal of Asian Earth Sciences, 173, 352–363.

Qu, K., Sima, X.Z., Gu, X.P., Sun, W.Z., Fan, G., Hou, Z.Q., Ni, P., Wang, D.M., Yang, Z.Q., and Wang, Y.J. (2021) Kenoargentotetrahedrite-(Zn), IMA 2020-075. CNMNC Newsletter 59. Mineralogical Magazine, 85, 278–281.

Qu, K., Sun, W.Z., Gu, X.P., Yang, Z.Q., Sima, X.Z., Tang, C., Fan, G., and Wang, Y.J.

(2022) Kenorozhdestvenskayaite-(Fe), IMA 2022-001. CNMNC Newsletter 67. Mineralogical Magazine, 86, 849–853.

Repstock, A., Voudouris, P., Zeug, M., Melfos, V., Zhai, M., Li, H., Kartal, T. and Matuszczak, J. (2016) Chemical composition and varieties of fahlore-group minerals from Oligocene mineralization in the Rhodope area, Southern Bulgaria and Northern Greece. Mineralogy and Petrology, 110, 103–123.

Rigaku Oxford Diffraction. (2021) CrysAlisPro Software system, version 1.171.41.96a. Rigaku Corporation.

Riley, J.F. (1974) The tetrahedrite–freibergite series, with reference to the Mount Isa Pb–Zn–Ag orebody. Mineralium Deposita, 9, 117–124.

Rozhdestvenskaya, I.V. (1993) Crystal structure features of minerals from a series of tetrahedrite-freibergite. Mineralogiceskij Zhurnal, 15, 9–17 (in Russian).

Sack, R.O., Lyubimtseva, N.G., Bortnikov, N.S., Anikina, E.Y., and Borisovsky, S.E. (2022) Sulfur vacancies in fahlores from the Ag-Pb–Zn Mangazeyskoye ore deposit (Sakha, Russia). Contributions to Mineralogy and Petrology, 177, 82.

Samusikov, V.P., Zayakina, N.V., and Leskova, N.V. (1988) Relation between unit cell of fahlores and Ag-concentration. Doklady Akademii Nauk USSR, 299, 468–471 (in Russian).

Sejkora, J., Biagioni, C., Vrtiška, L., and Moëlo, Y. (2021) Zvěstovite-(Zn), $Ag_6(Ag_4Zn_2)As_4S_{13}$, a new tetrahedrite-group mineral from Zvěstov, Czech Republic. Mineralogical Magazine, 85, 716–724.

Sejkora, J., Biagioni, C., Števko, M., Raber, T., Roth, P., and Vrtiška, L. (2022) Argentotetrahedrite-(Zn), $Ag_6(Cu_4Zn_2)Sb_4S_{13}$, a new member of the tetrahedrite group. Mineralogical Magazine, 86, 319–330.

Shannon, R.D. (1976) Revised effective ionic radii and systematic studies of interatomic distances in halides and chalcogenides. Acta crystallographica section A: crystal physics, diffraction, theoretical and general crystallography, 32, 751–767.

Sheldrick, G.M. (2015) SHELXT–Integrated space-group and crystal structure determination. Acta Crystallographica, A71, 3–8.

Toulmin, III.P., and Barton, Jr.P.B. (1964) A thermodynamic study of pyrite and pyrrhotite. Geochimica et Cosmochimica Acta, 28, 641–671.

Wang, M., Zhang, X., Guo, X., Pi, D., and Yang, M. (2018) Silver–bearing minerals in the Xinhua hydrothermal vein-type Pb-Zn deposit, South China. Mineralogy and Petrology, 112, 85–103.

Wang, Y.J., Chen, R.J., Gu, X.P., Nestola, F., Hou, Z.Q., Yang, Z.S., Dong, G.C., Guo, H., and Qu, K. (2023a) Tetrahedrite-(Ni), $Cu_6(Cu_4Ni_2)Sb_4S_{13}$, the first nickel member of tetrahedrite group mineral from Luobusa chromite deposits, Tibet, China. American Mineralogist. DOI: 10.2138/am-2022-8761.

Wang, Y.J., Chen, R.J., Gu, X.P., Hou, Z.Q., Nestola, F., Yang, Z.S., Fan, G., Dong, G.C., Ye, L.J., and Qu, K. (2023b) Tennantite-(Ni), $Cu_6(Cu_4Ni_2)As_4S_{13}$, from Luobusa ophiolite, Tibet, China: a new Ni-member of the tetrahedrite group. Mineralogical Magazine. 87, 591–598.

Wang, Z., Su, H.F., Kurmoo, M., Tung, C.H., Sun, D., and Zheng, L.S. (2018) Trapping an octahedral Ag_6 kernel in a seven-fold symmetric Ag_{56} nanowheel. Nature communications, 9, 2094.

Warr, L.N. (2021) IMA–CNMNC approved mineral symbols. Mineralogical Magazine, 85, 291–320.

Welch, M.D., Stanley, C.J., Spratt, J., and Mills, S.J. (2018) Rozhdestvenskayaite $Ag_{10}Zn_2Sb_4S_{13}$ and argentotetrahedrite $Ag_6Cu_4(Fe^{2+},Zn)_2Sb_4S_{13}$: two Ag-dominant members of the tetrahedrite group. European Journal of Mineralogy, 30, 1163–1172.

Zhang, H.F., Zhang, L., Gao, S., Zhang, B.R., and Wang, L.S. (1999) Pb isotopic compositions of metamorphic rocks and intrusive rocks in Tongbai region and their geological implication. Earth Science, 24, 269–273 (in Chinese with English abstract).

Zhang, H.F., Gao, S., Zhang, L., Zhong, Z.Q., and Zhang, B.R. (2000) Granitoids in Erlangping ophiolite fragment from northern Tongbai area, China: geochemistry, petrogenesis and deep crustal nature. Chinese Journal of Geology, 35, 27–39 (in Chinese with English abstract).

Zhang, J., Chen, Y.J., Qi, J.P., and Ge, J. (2009) Comparison of the typical metallogenic systems in the North slope of the Tongbai-East Qinling Mountains and its geologic implications. Acta Geologica Sinica-English Edition, 83, 396–410.

Zhang, J., Chen, Y., Yang, Y., and Deng, J. (2011) Lead isotope systematics of the Weishancheng Au-Ag belt, Tongbai Mountains, central China: implication for ore genesis. International Geology Review, 53, 656–676.

Zhang, J., Chen, Y.J., Pirajno, F., Deng, J., Chen, H.Y., and Wang, C.M. (2013) Geology, C–H–O–S–Pb isotope systematics and geochronology of the Yindongpo gold deposit, Tongbai Mountains, central China: Implication for ore genesis. Ore Geology Reviews, 53, 343–356.

Zeng, W., Duan, M., Wan, D., Sima, X.Z., Ao, C., Ren, Aiqing., Yang, Z.Q., and Li, F.L. (2016) Ore-forming Fluids and Genesis of Yindongpo Gold Deposit, Henan Province. Geoscience, 30, 781–791(in Chinese with English abstract).

Table Captions

TABLE 1 – Chemical data (wt. %) for kenorozhdestvenskayaite-(Fe)

TABLE 2 – Calculated X-ray powder diffraction data (*d* in Å) for kenorozhdestvenskayaite-(Fe)

TABLE 3 – Comparative characteristics of kenorozhdestvenskayaite, kenoargentotetrahedrite, and rozhdestvenskayaite

TABLE 4 – Bond-valence (*v.u.*) calculation for kenorozhdestvenskayaite-(Fe)

TABLE 5 – Structural comparison between synthetic $Ag_6Ge_{10}P_{12}$ and kenorozhdestvenskayaite-(Fe)

TABLE 6 – Component of pyrrhotite (at. %) and related thermodynamic quantities

Figure Captions

FIGURE 1 – (a-b) Schematic tectonic map of China showing the Central China Orogenic Belt (modified after Qu et al. 2019); (c) geological sketch of the Weishancheng ore district and the distribution of ore deposits (after Zhang et al. 2011); (d) simplified geological map of the Yindongpo Au deposit (modified from Zhang et al. 2009).

FIGURE 2 – Backscattered electron (BSE) images of the occurrence and mineral association of kenorozhdestvenskayaite-(Fe). Mineral symbols are quoted from Warr (2021).

(**a**) Subhedral kenorozhdestvenskayaite-(Fe) (Kroz-Fe) associated with sphalerite (Sp), galena (Gn), pyrite (Py) and pyrrhotite (Pyh).

(**b**) Kenorozhdestvenskayaite-(Fe) occurring in galena as small composite inclusions composed of pyrargyrite (Pyg), associated with sphalerite and siderite (Sd) matrix.

(**c**) Anhedral kenorozhdestvenskayaite-(Fe) occurring with galena, sphalerite, and pyrrhotite.

(**d**) Euhedral kenoargentotetrahedrite-(Fe) (Kattr-Fe) formed along the edges of galena, and kenoargentotetrahedrite-(Fe) that was partially altered by the secondary unknown Ag-I phase (Ag_6S_2).

(**e**) Kenorozhdestvenskayaite-(Fe) associated with sphalerite, galena, chalcopyrite (Ccp), pyrrhotite, unknown Ag-I phase, and kutnohorite (Kut).

(**f**) Kenoargentotetrahedrite-(Zn) (Kattr-Zn) occurring with sphalerite, galena, rhodochrosite (Rds) and an unknown Ag-II phase (Ag_6AgSbS_4).

539

540 **FIGURE 3** – Raman spectrum of kenorozhdestvenskayaite-(Fe).

541

542 **FIGURE 4** – Crystal structure of kenorozhdestvenskayaite-(Fe), plotted using the Olex2
543 software (Dolomanov et al. 2009).

544

545 **FIGURE 5** – Perspective representation of the $[Ag_6]^{4+}$ cluster for
546 kenorozhdestvenskayaite-(Fe), plotted using the VESTA software (Momma and Izumi
547 2011).

TABLE 1. Chemical data (wt. %) for kenorozhdestvenskayaite-(Fe)

Element	mean (%)	range (%)	S.D. (σ)	*apfu*
Ag	45.87	43.32–47.46	1.46	8.41
Cu	3.87	2.73–5.14	0.92	1.20
Fe	5.18	5.07–5.28	0.08	1.84
Zn	2.36	1.84–2.95	0.38	0.71
Sb	23.52	22.82–24.12	0.46	3.82
As	0.04	0.00–0.07	0.03	0.01
S	18.80	18.24–19.09	0.31	11.60
Total	99.62			

S.D. = standard deviation.

TABLE 2. Caluculated X-ray powder diffraction data (*d* in Å) for kenorozhdestvenskayaite-(Fe)

I_{cal}	d_{calc}	*h k l*
28	**7.5745**	**1 1 0**
9	4.3731	2 1 1
9	3.7872	2 2 0
100	**3.0923**	**2 2 2**
4	2.8629	3 2 1
43	**2.6780**	**4 0 0**
12	**2.5248**	**3 3 0**
9	2.2838	3 3 2
12	**2.1008**	**4 3 1**
7	1.9557	5 2 1
27	**1.8936**	**4 4 0**
7	1.7377	6 1 1
7	1.6937	6 2 0
15	**1.6149**	**6 2 2**

Note: Only reflections with $I_{calc} > 4$ are listed. The seven strongest reflections are given in bold.

TABLE 3. Comparative characteristics of kenorozhdestvenskayaite, kenoargentotetrahedrite, and rozhdestvenskayaite.

	Kenorozhdestvenskayaite-(Fe)	Kenoargentotetrahedrite-(Fe)†	Kenoargentotetrahedrite-(Zn)*	Rozhdestvenskayaite-(Zn)‡
Ideal formula	$Ag_6(Ag_4Fe_2)Sb_4S_{12}\square$	$Ag_6(Cu_4Fe_2)Sb_4S_{12}\square$	$Ag_6(Cu_4Zn_2)Sb_4S_{12}\square$	$Ag_6(Ag_4Zn_2)Sb_4S_{13}$
Crystal system	cubic	cubic	cubic	cubic
Space group	$I\bar{4}3m$	$I\bar{4}3m$	$I\bar{4}3m$	$I\bar{4}3m$
a(Å)	10.7119(6)	10.4930(4)	10.4624(4)	10.9845(7)
V(Å^3)	1229.1(2)	1155.31(8)	1145.23(8)	1325.37(15)
Z	2	2	2	2
$M(2)_6$	$[Ag_6]^{4+}$	$[Ag_6]^{4+}$	$[Ag_6]^{4+}$	$(Ag_6)^{6+}$
M(2) site (occ.)	$Ag_{0.9}Cu_{0.1}$	$Ag_{0.88}Cu_{0.12}$	$Ag_{0.63}Cu_{0.37}$	Ag
M(1) site (occ.)	$Ag_{0.54}Cu_{0.12}Fe_{0.24}Zn_{0.1}$	Cu	$Cu_{0.65}Zn_{0.21}Fe_{0.14}$	$Ag_{0.75}Cu_{0.25}$
X(3) site (occ.)	Sb	Sb	$Sb_{0.97}As_{0.03}$	Sb
S(1) site (occ.)	S	S	S	S
S(2) site (occ.)	$\square_{0.9}S_{0.1}$	$\square$	$\square_{0.63}S_{0.37}$	S
Ag–Ag distance(Å)	2.844(4)	2.841(2)	2.890(2)	3.230(4)
M(2)–centroid or *M*(2)–S2 bond(Å)	2.011(3)	2.009	2.043(2)	2.284(3)
M(2)–S2 Vol. (Å^3)	10.84	10.81	11.38	15.88
M(2)–S1 bond (Å)	2.550(6)	2.554(2)	2.475(4)	2.500(3)
M(1)–S1 bond (Å)	2.439(4)	2.333(1)	2.343(2)	2.496(2)
X(3)–S1 bond (Å)	2.428(6)	2.434(2)	2.441(4)	2.425(3)

Notes: †Kenoargentotetrahedrite-(Fe) named as "freibergite" and ‡ rozhdestvenskayaite-(Zn) named as "rozhdestvenskayaite" in Welch et al (2018), both renamed by Biagioni et al (2020); * Qu et al (2021).

TABLE 4. Bond-valence (*vu*) calculation for kenorozhdestvenskayaite-(Fe)

Site	*M*(2) ($Ag_{0.90(3)}Cu_{0.10(3)}$)	*M*(1) ($Ag_{0.54}Cu_{0.12}Fe_{0.24}Zn_{0.10}$)	*X*(3) (Sb)	Sum.	Theor.
S(1)	$0.321^{\times 2\downarrow}$	$0.424^{\times 4\downarrow \times 2\rightarrow}$	$1.061^{\times 3\downarrow}$	2.230	2.000
Sum.	0.642	1.697	3.184		
Theor.	0.667†	1.333	3.000		

Notes: Bond valence sums were calculated with the site-occupancy factors. Calculations were using the bond-valence parameters of Brese and O'Keeffe (1991), and the equation and constants of Brown (1977), $S = \exp[(R_0 - d_0)/b]$. †The theoretical bond valence of *M*(2) site is based on the $[Ag_6]^{4+}$.

TABLE 5. Structural comparison between synthetic $Ag_6Ge_{10}P_{12}$ and kenorozhdestvenskayaite-(Fe)

Wyckoff	$Ag_6Ge_6Ge_4P_{12}\square$ †	$Ag_6(Ag_4Fe_2)Sb_4S_{12}\square$ ‡
12*e*	$Ag^{0.67+}$	$^{M(2)}Ag^{0.67+}$
12*d*	Ge^{4+}	$^{M(1)}[Ag_{2/3}Fe_{1/3}]^{1.33+}$
8*c*	Ge^{2+}	$^{X(3)}Sb^{4+}$
24*g*	P^{3-}	$^{S(1)}S^{2-}$
2*a*	□	$^{S(2)}\square$
Crystal system	cubic	cubic
Space group	$I\bar{4}3m$	$I\bar{4}3m$
a(Å)	10.2959(13)	10.7119(6)
V(Å^3)	1091.4(2)	1229.1(2)
Ag-Ag distance(Å)	2.8379(7)	2.844(4)
Ag-centroid distance(Å)	2.007(5)	2.011(3)
$[Ag_6]^{4+}$ cluster Vol. (Å^3)	10.77	10.84

Notes: † synthetic $Ag_6Ge_{10}P_{12}$, Nuss et al. (2017); ‡ kenorozhdestvenskayaite-(Fe), this study

TABLE 6. Component of pyrrhotite (at. %) and related thermodynamic quantities

Point	Fe	S	N	$\log f_{S2}$
1	46.6	53.4	0.932	–8.83
2	46.9	53.1	0.938	–9.66
3	46.8	53.2	0.936	–9.38
4	47.1	52.9	0.942	–10.23
5	47.5	52.5	0.95	–11.40
6	47.4	52.6	0.948	–11.10
7	47	53	0.94	–9.94
8	46.9	53.1	0.938	–9.66
min	46.6	52.5	0.932	–11.40
max	47.5	53.4	0.95	–8.83
mean	47.03	52.98	0.941	–10.03
S.D	0.30	0.30	0.01	0.86

Notes: $\log f_{S2} = (70.03 - 85.83N)(1000/T - 1) + 39.30\sqrt{1\text{-}0.9981N} - 11.91$ (Toulmin and Barton 1964), $N = 2\left(\frac{nFe}{nFe+nS}\right)$, T = 573.15 K (referring to Zhang et al. 2013 about the fluid inclusion temperature of the second ore-forming stage), S.D = standard deviation.

Figure 1

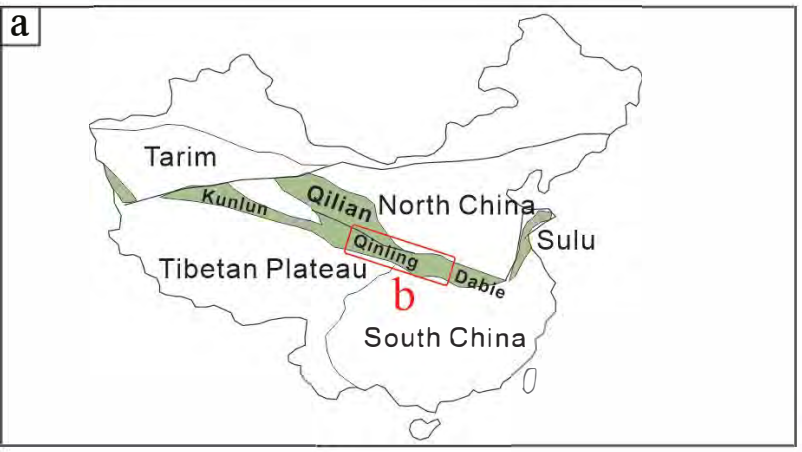
a
Tarim
Kunlun
Qilian
North China
Qinling
Dabie
Sulu
Tibetan Plateau
b
South China

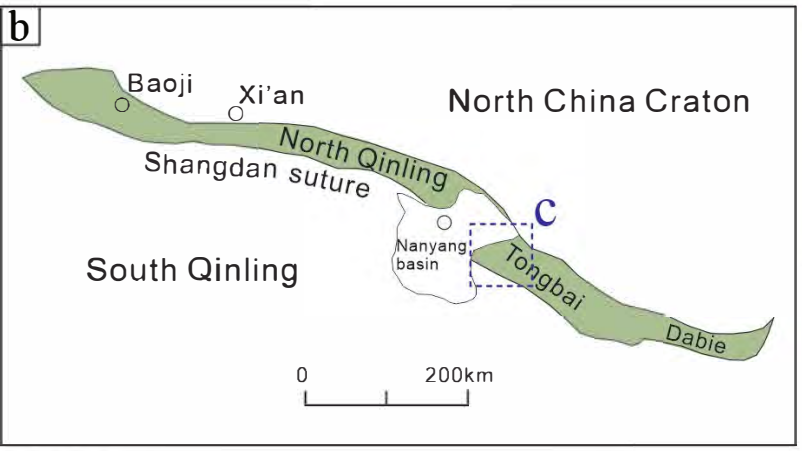
b
Baoji
Xi'an
North China Craton
North Qinling
Shangdan suture
c
Nanyang basin
Tongbai
Dabie
South Qinling
0
200km

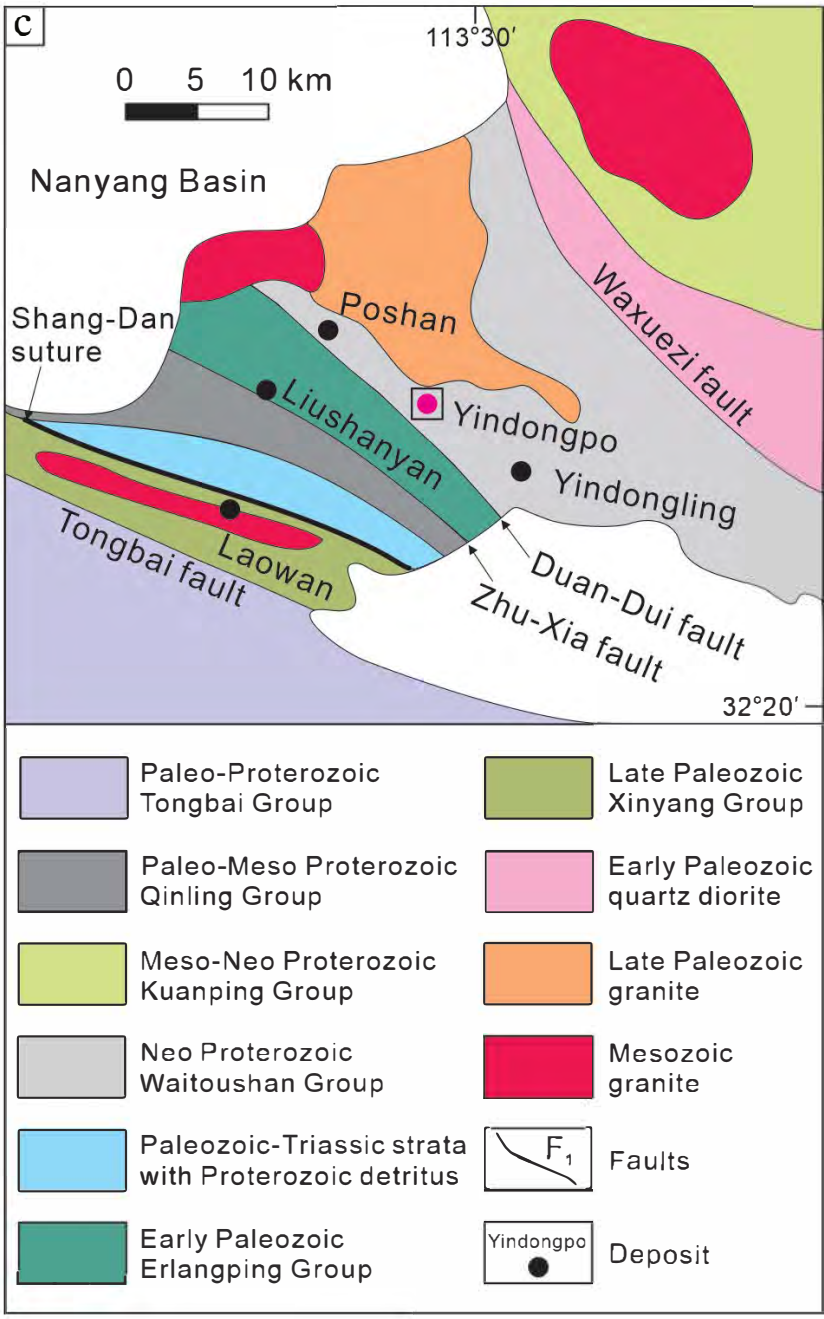
c
113°30′
0 5 10 km
Nanyang Basin
Shang-Dan suture
Poshan
Waxuezi fault
Liushanyan
Yindongpo
Yindongling
Tongbai fault
Laowan
Duan-Dui fault
Zhu-Xia fault
32°20′
Paleo-Proterozoic Tongbai Group
Paleo-Meso Proterozoic Qinling Group
Meso-Neo Proterozoic Kuanping Group
Neo Proterozoic Waitoushan Group
Paleozoic-Triassic strata with Proterozoic detritus
Early Paleozoic Erlangping Group
Late Paleozoic Xinyang Group
Early Paleozoic quartz diorite
Late Paleozoic granite
Mesozoic granite
F1
Faults
Yindongpo
Deposit

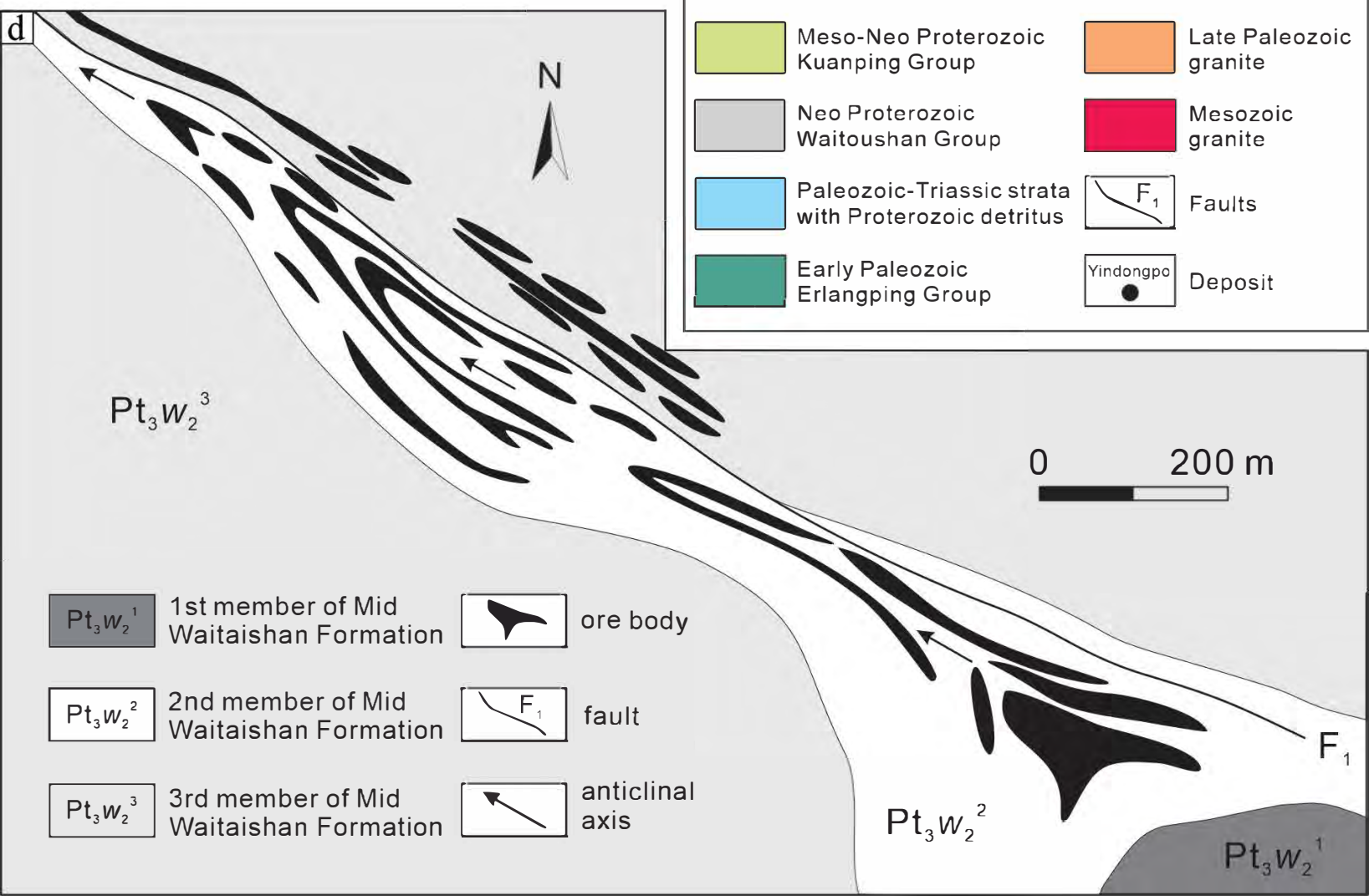
d
N
Pt3w2 3
0 200 m
Pt3w2 1
1st member of Mid Waitaishan Formation
Pt3w2 2
2nd member of Mid Waitaishan Formation
Pt3w2 3
3rd member of Mid Waitaishan Formation
ore body
F1
fault
anticlinal axis
F1
Pt3w2 2
Pt3w2 1

Figure 2

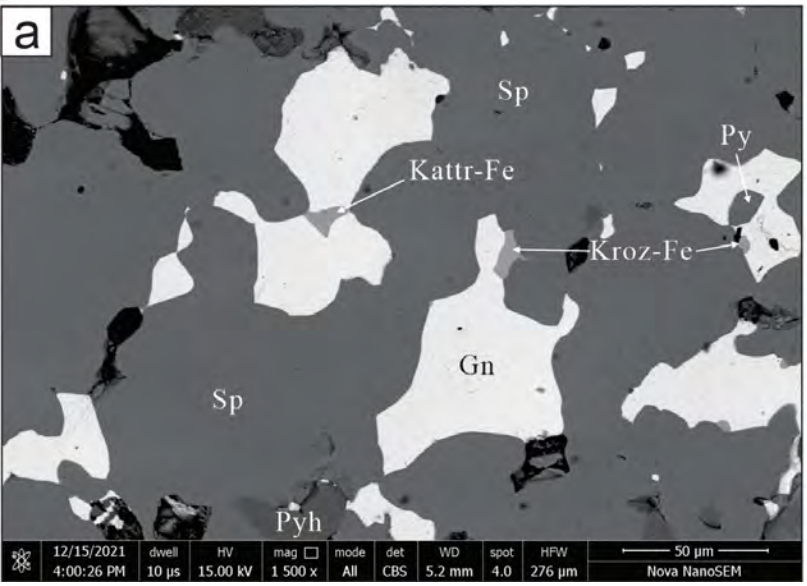
a
Sp
Py
Kattr-Fe
Kroz-Fe
Gn
Sp
Pyh
12/15/2021 4:00:26 PM dwell 10 µs HV 15.00 kV mag 1 500 x mode All det CBS WD 5.2 mm spot 4.0 HFW 276 µm 50 µm Nova NanoSEM

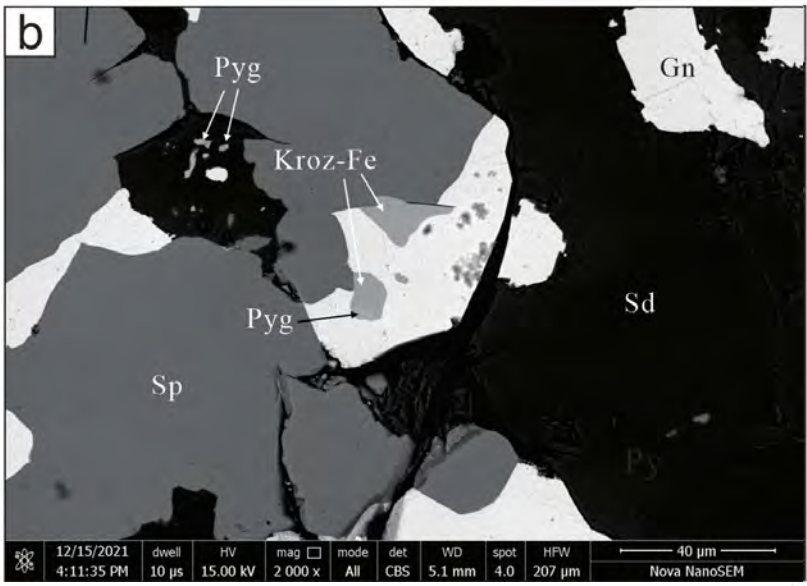
b
Pyg
Gn
Kroz-Fe
Pyg
Sd
Sp
Py
12/15/2021 4:11:35 PM dwell 10 µs HV 15.00 kV mag 2 000 x mode All det CBS WD 5.1 mm spot 4.0 HFW 207 µm 40 µm Nova NanoSEM

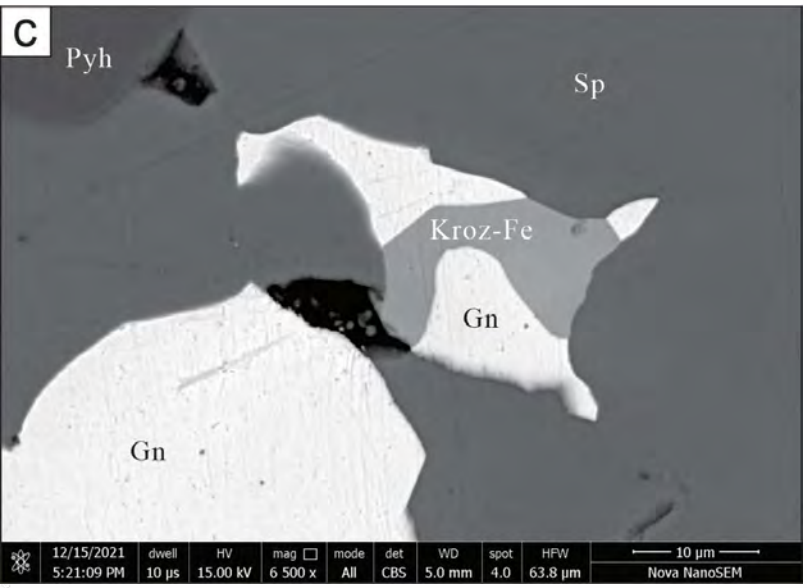
c
Pyh
Sp
Kroz-Fe
Gn
Gn
12/15/2021 5:21:09 PM dwell 10 µs HV 15.00 kV mag 6 500 x mode All det CBS WD 5.0 mm spot 4.0 HFW 63.8 µm 10 µm Nova NanoSEM

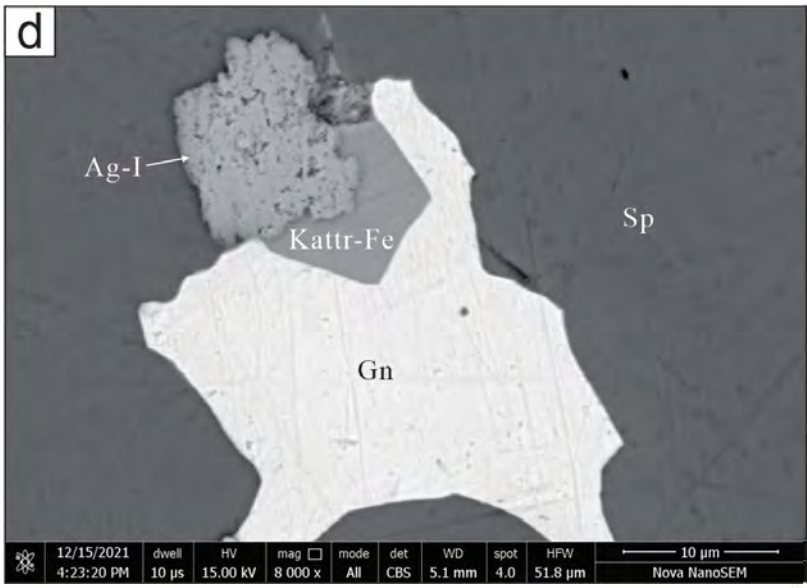
d
Ag-I
Sp
Kattr-Fe
Gn
12/15/2021 4:23:20 PM dwell 10 µs HV 15.00 kV mag 8 000 x mode All det CBS WD 5.1 mm spot 4.0 HFW 51.8 µm 10 µm Nova NanoSEM

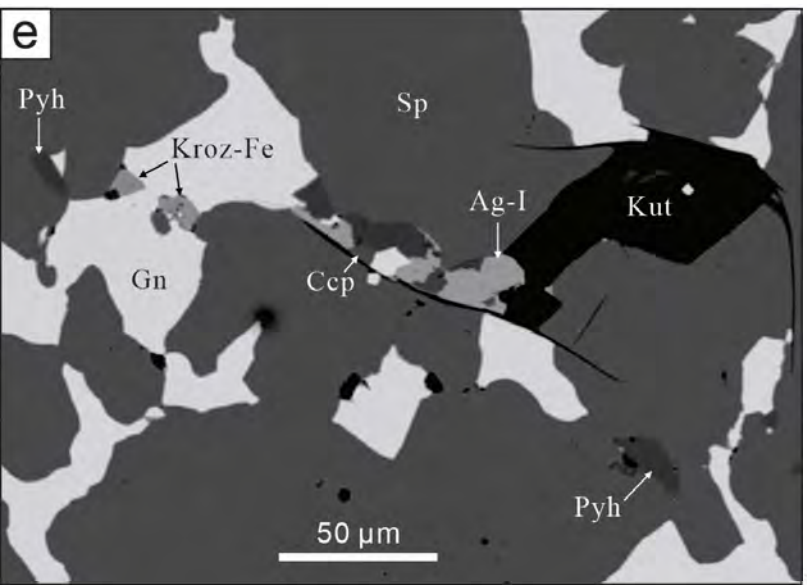
e
Pyh
Sp
Kroz-Fe
Ag-I
Kut
Gn
Ccp
Pyh
50 µm

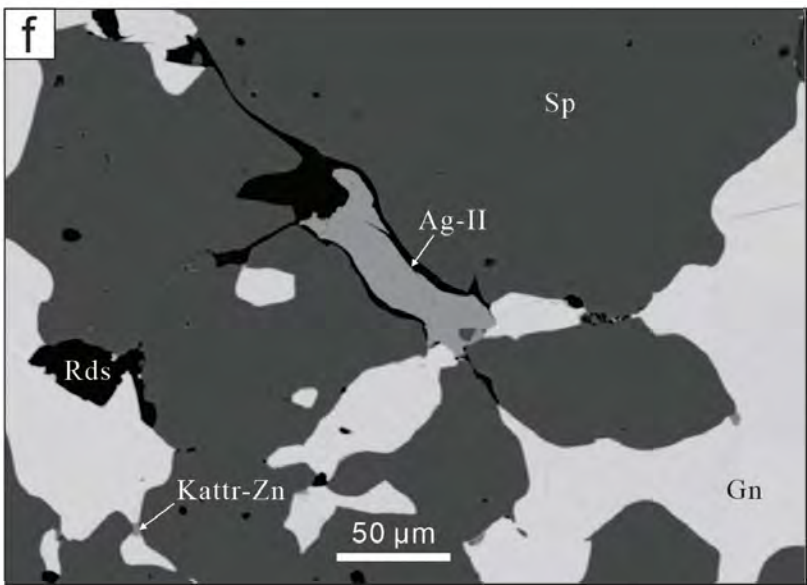
f
Sp
Ag-II
Rds
Kattr-Zn
Gn
50 µm

Figure 3

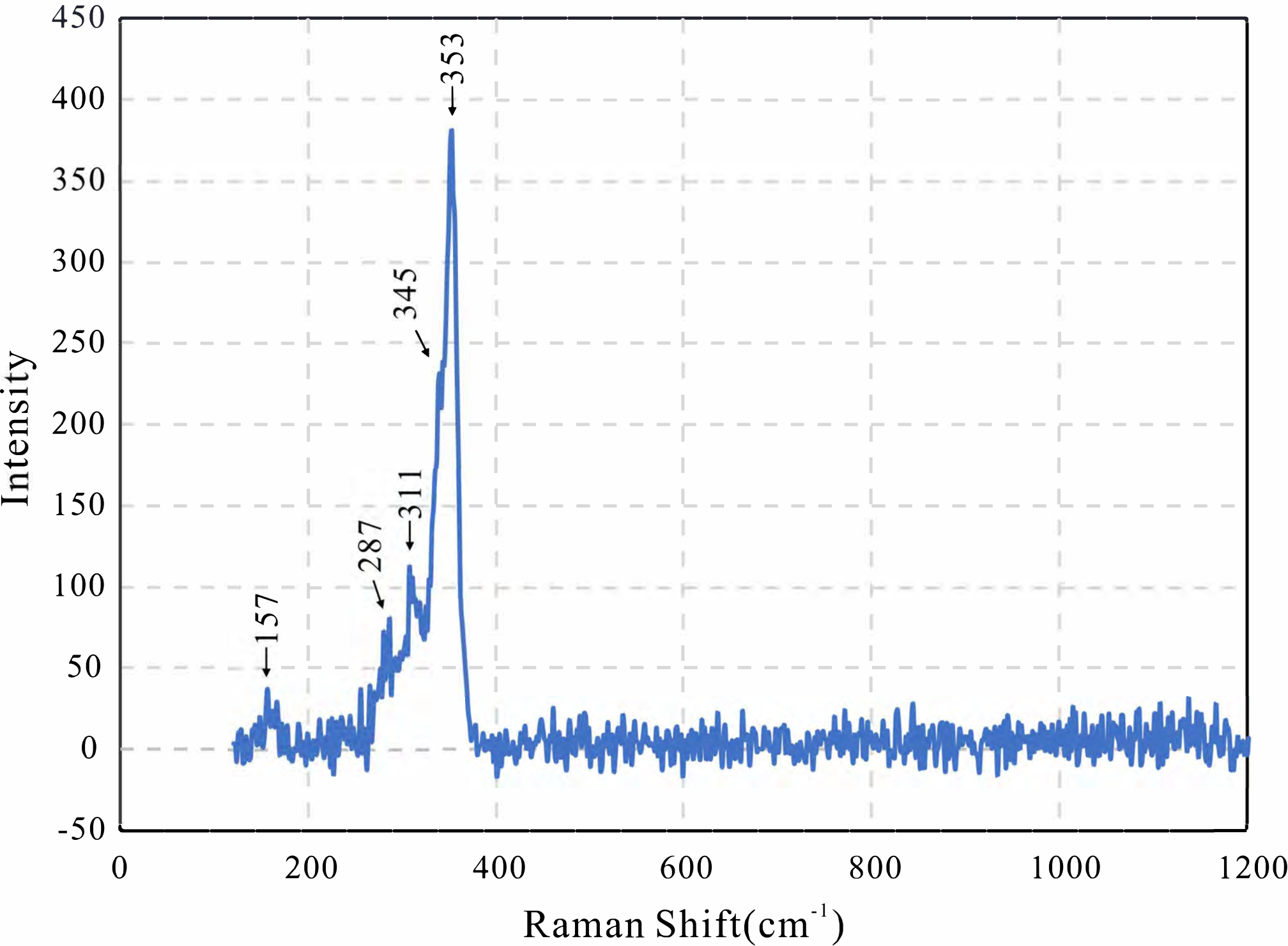
450
400
350
300
250
200
150
100
50
0
-50
Intensity
0
200
400
600
800
1000
1200
Raman Shift(cm-1)
157
287
311
345
353

Figure 4

$M(1) = \frac{2}{3}Ag^{+} + \frac{1}{3}Fe^{2+}$

$M(2) = Ag^{2/3+}$

$X(3) = Sb^{3+}$

$S(1) = S^{2-}$

$S(2) = \square$

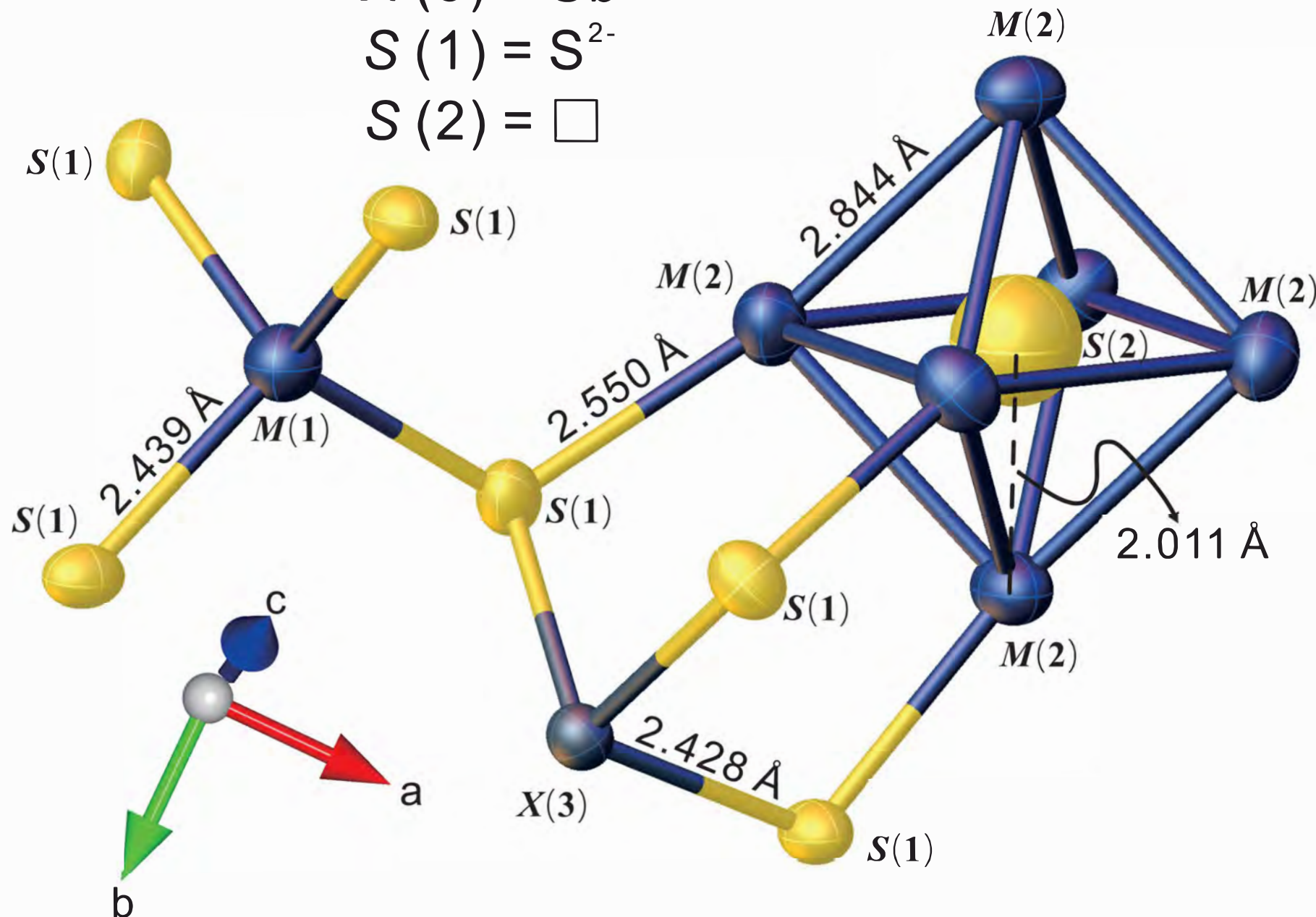

Figure 5